

# Electron and proton storage on separate Ru and BaO domains mediated by conductive low-work-function carbon to accelerate ammonia synthesis

Received: 21 July 2024

Accepted: 30 January 2025

Published online: 24 February 2025



Yaejun Baik<sup>1</sup>, Seunghyuck Chi<sup>1</sup>, Kyeongjin Lee<sup>1</sup>, DongHwan Oh<sup>1</sup>,  
Kyungho Lee<sup>2</sup> & Minkee Choi<sup>1</sup>✉

Ammonia (NH<sub>3</sub>) has gained attention as a carbon-free fuel and hydrogen carrier, making its energy-efficient production increasingly important. Here we demonstrate that Ru and BaO, connected by conductive carbon, can separately store e<sup>−</sup> and H<sup>+</sup>, like a chemical capacitor under NH<sub>3</sub> synthesis conditions. H atoms generated on the Ru surface by H<sub>2</sub> activation polarize into H<sup>+</sup>/e<sup>−</sup> pairs. Subsequently, H<sup>+</sup> migrates over the carbon surfaces to neutralize basic BaO, while e<sup>−</sup> accumulates in conductive Ru/carbon. As the work function of carbon decreases, Ru gradually becomes enriched with e<sup>−</sup>, facilitating N<sub>2</sub> activation via  $\pi$ -backdonation and alleviating H<sub>2</sub> poisoning. Thus, an optimized catalyst synthesized using N-doped MWNT with the lowest work function, exhibited 7.4 times higher activity than a reference Ba–Ru/MgO catalyst. The results show that charge distribution within catalysts can be markedly altered under reaction conditions, and its rational control can enable the design of active NH<sub>3</sub> synthesis catalysts.

Ammonia (NH<sub>3</sub>) is essential for the production of fertilizers, pharmaceuticals and explosives, and it has recently gained attention as a carbon-free fuel and a hydrogen carrier<sup>1,2</sup>. Conventional NH<sub>3</sub> synthesis via the Haber–Bosch process relies on fossil-derived H<sub>2</sub>, operates under harsh conditions (>723 K, >15 MPa) and necessitates centralized facilities for economic viability<sup>3,4</sup>. This process contributes over 1.2% of the global anthropogenic CO<sub>2</sub> emissions and incurs additional costs for transportation and distribution<sup>3,4</sup>. As a more sustainable alternative, decentralized NH<sub>3</sub> synthesis coupled with renewable H<sub>2</sub> production has garnered scientific attention<sup>5,6</sup>. To integrate with electrolytic H<sub>2</sub> production and achieve greater economic feasibility, NH<sub>3</sub> synthesis under much milder conditions (<573 K, <2 MPa) is desirable<sup>6</sup>. The major challenge of NH<sub>3</sub> synthesis under such conditions lies in activating the stable N≡N bonds (945 kJ mol<sup>−1</sup>) of N<sub>2</sub>, necessitating the development of more advanced catalysts<sup>7</sup>.

Ru catalysts, often supported on MgO (refs. 8–13) and carbon<sup>14–20</sup> in combination with base promoters (for example, Ba, Cs and La oxides), have exhibited high NH<sub>3</sub> synthesis activities under mild conditions<sup>21</sup>. Consequently, the base-promoted Ru catalysts were commercialized through the Kellogg Advanced Ammonia Process in the mid-1990s<sup>22</sup>. The catalytic effect of base promoters is known to be crucial, often increasing NH<sub>3</sub> synthesis activities by an order of magnitude<sup>8–12,15,16</sup>. It has been generally speculated that promoters can influence Ru particle sizes to increase the number of active step sites (known as B<sub>5</sub> sites)<sup>11,18</sup> or donate electrons to Ru (refs. 9,16). Although the underlying reasons remain elusive, the promotional effects vary substantially depending on the types of supports, loadings of promoters and synthesis methods<sup>8–11,13,15,16</sup>.

Recently, we elucidated the role of base promoters using well-defined Ba–Ru/MgO catalysts with a fixed Ru dispersion but

<sup>1</sup>Department of Chemical and Biomolecular Engineering (BK21 Four), Korea Advanced Institute of Science and Technology, Daejeon, Republic of Korea.

<sup>2</sup>Clean Fuel Research Laboratory, Korea Institute of Energy Research, Daejeon, Republic of Korea. ✉e-mail: [mkchoi@kaist.ac.kr](mailto:mkchoi@kaist.ac.kr)

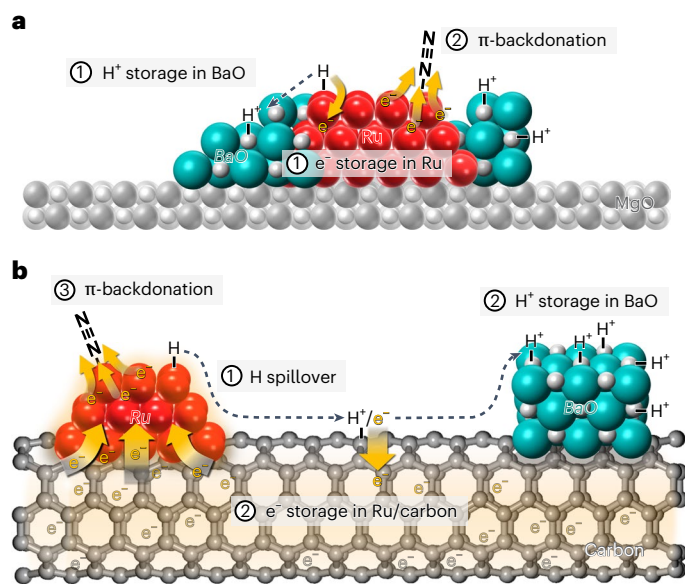


**Fig. 1 | Hydrogen-aided electron donation of BaO to Ru during NH<sub>3</sub> synthesis.** **a**, BaO-promoted Ru catalysts on an insulating MgO support. Chemisorbed H atoms on Ru polarize into H<sup>+</sup>/e<sup>-</sup> pairs at the BaO–Ru interfaces, where non-reducible BaO selectively captures H<sup>+</sup> while leaving e<sup>-</sup> in Ru. **b**, BaO-promoted Ru catalysts on a conductive carbon support. H<sup>+</sup>/e<sup>-</sup> pairs can migrate over long distances across the carbon surface. BaO can capture H<sup>+</sup> even without direct contact with Ru, while accumulating e<sup>-</sup> in the conductive Ru/carbon.

varying interface formation between Ru and BaO (ref. 8). Rigorous analyses revealed that BaO donates electrons (e<sup>-</sup>) to Ru not through simple inductive effects<sup>9,16</sup>, but rather via a unique mechanism aided by H<sub>2</sub> under reductive reaction conditions (Fig. 1a). When H<sub>2</sub> is activated on Ru, the resulting H atoms dissociate into H<sup>+</sup>/e<sup>-</sup> pairs at the BaO–Ru interfaces. The strongly basic, non-reducible BaO selectively captures H<sup>+</sup>, while leaving e<sup>-</sup> in Ru. The resulting e<sup>-</sup> enrichment of Ru facilitates N<sub>2</sub> activation through enhanced π-backdonation and suppresses H<sub>2</sub> poisoning, increasing NH<sub>3</sub> synthesis activities. Because the insulating MgO support prevents the long-range migration of H<sup>+</sup>/e<sup>-</sup> pairs (or H spillover), such phenomena occur only at the intimate BaO–Ru interfaces. This implies that enlarging the BaO–Ru interface is necessary to achieve high catalytic activity. However, excessive BaO loading also results in blockage of active Ru sites by BaO, causing a trade-off between specific activity and the number of sites<sup>8</sup>.

We hypothesize that the aforementioned trade-off in catalyst design can be overcome by using conductive supports such as carbon. Carbon is known to facilitate the long-range migration of H<sup>+</sup>/e<sup>-</sup> pairs (or H spillover), with H<sup>+</sup> migrating over its surface and e<sup>-</sup> travelling through the conduction band<sup>23–25</sup>. This implies that BaO on carbon can capture H<sup>+</sup> even without direct contact with Ru, while leaving e<sup>-</sup> in the conductive Ru/carbon (Fig. 1b). This can induce e<sup>-</sup> enrichment of Ru without its surface blockage by BaO. Moreover, carbon can have a wide range of work functions (4.3–6.5 eV), which vary depending on nanostructures and heteroatom doping<sup>26–30</sup>. If carbon can be designed to have a lower work function than Ru (–4.7 eV)<sup>31</sup>, preferential e<sup>-</sup> transfer from carbon to Ru can be further anticipated. Compared with various low-work-function supports used to increase the NH<sub>3</sub> synthesis activity of Ru (for example, electrides<sup>32–34</sup>, hydrides<sup>35,36</sup> and amides<sup>37,38</sup>), carbon can offer advantages in terms of air stability, material cost and production scalability.

In this study, we demonstrate that Ba–Ru/carbon catalysts can exhibit remarkably different NH<sub>3</sub> synthesis properties depending on the types of carbon supports, and indeed their work functions govern the overall catalytic properties. Consequently, N-doped multiwalled carbon nanotube with the lowest work function could yield a catalyst

with high NH<sub>3</sub> synthesis activity at 573 K and 10 bar, which is 7.4 times higher than a benchmark Ba–Ru/MgO catalyst.

## Results

### Synthesis and characterizations of Ba–Ru/carbon catalysts

We used 11 carbon supports after acid washing to remove metal impurities: activated carbon (AC), graphene, graphite, graphitic carbon nanofibre (GNF), single-walled carbon nanotube (SWNT), double-walled carbon nanotube (DWNT), multiwalled carbon nanotubes with diameters of 10–20 nm (MWNT-1), 20–30 nm (MWNT-2), 30–50 nm (MWNT-3) and 50–80 nm (MWNT-4), and N-doped MWNT-1 (N-MWNT-1). The properties of carbon supports are summarized in Supplementary Fig. 1 and Supplementary Table 1. Onto the supports, 5 wt% Ru was supported by the impregnation of a RuCl<sub>3</sub> solution and subsequent reduction in H<sub>2</sub> at 673 K. The resulting Ru/carbon catalysts were further impregnated with Ba(NO<sub>3</sub>)<sub>2</sub> and treated in H<sub>2</sub> at 673 K to produce Ba–Ru/carbon catalysts, containing ~4.8 wt% Ru with a molar Ba/Ru ratio of 0.75 (Supplementary Table 2). For comparison, Ru/MgO and Ba–Ru/MgO catalysts were also prepared with the same Ru and Ba contents using the optimized method we previously reported<sup>8</sup>. According to transmission electron microscopy (TEM) (Supplementary Figs. 2 and 3) and CO chemisorption (Supplementary Table 2), all catalysts contained Ru particles with similar sizes (2.1–2.4 nm). This corresponds to the optimal size distribution of Ru particles (1.8–2.5 nm) for maximizing the number of active B<sub>5</sub> sites<sup>39–41</sup>. Because all catalysts have comparable Ru dispersions, the catalytic effects due to different particle sizes (geometric effects) can be ignored in the subsequent experiments.

High-angle annular dark-field scanning TEM (HAADF-STEM) and elemental mapping via energy-dispersive spectroscopy revealed that Ba–Ru/carbon and Ba–Ru/MgO catalysts have completely different locations and dispersions of BaO. In Ba–Ru/carbon catalysts, island BaO domains larger than 10 nm were predominantly formed and most of the small Ru particles were not in contact with BaO (Fig. 2a and Supplementary Figs. 4 and 5). Due to the low BaO dispersions, all Ba–Ru/carbon catalysts exhibited strong characteristic peaks for BaO on X-ray diffraction (XRD) (Supplementary Fig. 6). By contrast, Ba–Ru/MgO exhibited efficient formation of BaO–Ru interfaces (Fig. 2b); subnanometre BaO domains were primarily located near the Ru particles. Due to the high BaO dispersion, this catalyst did not show characteristic peaks for BaO in XRD (Supplementary Fig. 6). The distinct dispersion and location of basic BaO were further confirmed by temperature-programmed desorption mass spectrometry using acidic CO<sub>2</sub> as a probe (CO<sub>2</sub> TPD–MS). All Ba–Ru/carbon catalysts exhibited a strong peak centred at 1,000–1,030 K, with a tail extending up to 1,273 K (Fig. 2c). This peak can be assigned to the desorption of CO<sub>2</sub> from the island BaO domains (Supplementary Fig. 7), indicating a very strong interaction between the highly basic island BaO domains and acidic CO<sub>2</sub>. The catalysts also exhibited weaker desorption peaks at 700–760 K due to the decomposition of surface carboxyl groups on carbon<sup>42</sup>. These peaks were observed even without CO<sub>2</sub> preadsorption on the catalysts (Supplementary Fig. 8), and AC with the highest oxygen content gave the largest peak. Meanwhile, Ba–Ru/MgO exhibited a major CO<sub>2</sub> desorption peak at ~600 K (Fig. 2c), which was assigned to CO<sub>2</sub> desorption from the BaO–Ru interfaces<sup>8</sup>.

To understand the origin of the different BaO distributions in Ba–Ru/carbon and Ba–Ru/MgO catalysts, temperature-programmed reduction mass spectrometry (TPR–MS) was conducted after impregnating Ba(NO<sub>3</sub>)<sub>2</sub> onto carbon and MgO supports with and without Ru (Fig. 2d). TPR–MS results revealed that Ba(NO<sub>3</sub>)<sub>2</sub> decomposed into BaO with the generation of H<sub>2</sub>O and NH<sub>3</sub> in an H<sub>2</sub> atmosphere (Supplementary Fig. 9). On both Ru-free carbon and MgO surfaces, thermal decomposition of Ba(NO<sub>3</sub>)<sub>2</sub> occurred at 713–720 K. On Ru/MgO, Ba(NO<sub>3</sub>)<sub>2</sub> decomposition occurred at a lower temperature of 537 K, indicating that Ru can catalyse the decomposition of Ba(NO<sub>3</sub>)<sub>2</sub>. As insulating MgO

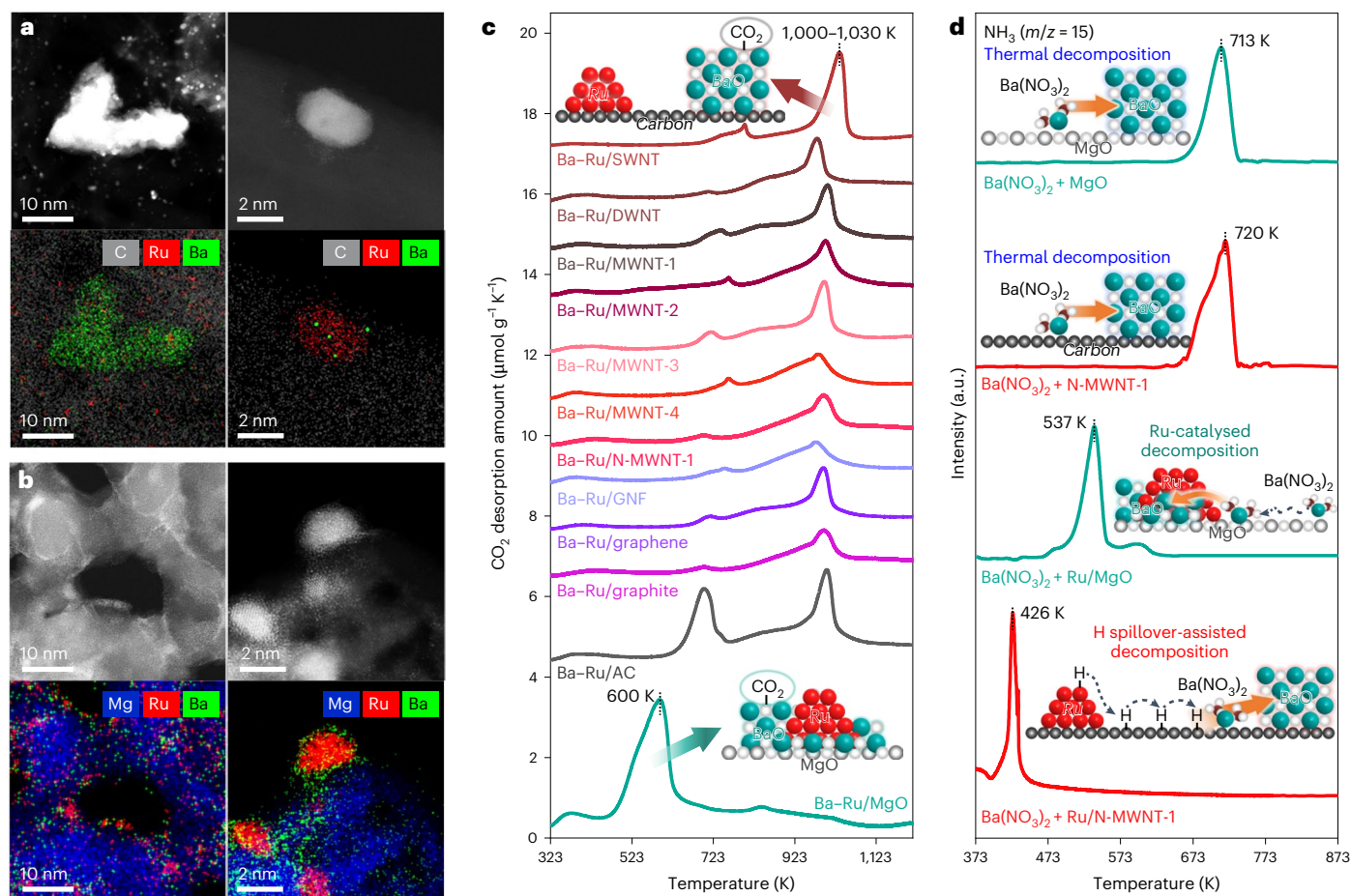


**Fig. 2 | Synthesis and characterization of Ba-Ru/carbon catalysts. a, b,** HAADF-STEM images and elemental mappings of Ba-Ru/N-MWNT-1 (a) and Ba-Ru/MgO (b). **c,** CO<sub>2</sub> TPD-MS profiles of Ba-Ru/carbon and Ba-Ru/MgO catalysts. Before

measurement, the samples were pretreated in He at 673 K, adsorbed with CO<sub>2</sub> at 323 K and purged with He at 323 K to remove weakly adsorbed CO<sub>2</sub>. **d,** TPR-MS profiles of Ba(NO<sub>3</sub>)<sub>2</sub>-impregnated MgO, N-MWNT-1, Ru/MgO and Ru/N-MWNT-1.

does not enable H spillover<sup>43,44</sup>, the possibility of Ba(NO<sub>3</sub>)<sub>2</sub> decomposition via H spillover can be excluded. Such Ru-catalysed Ba(NO<sub>3</sub>)<sub>2</sub> decomposition results in the formation of BaO in close proximity to Ru particles<sup>8</sup>, forming intimate BaO–Ru interfaces (Fig. 2b). On Ru/carbon surface, Ba(NO<sub>3</sub>)<sub>2</sub> decomposition occurred at further reduced temperatures (426 K; Fig. 2d). We believe that Ba(NO<sub>3</sub>)<sub>2</sub> could decompose at such low temperatures via H spillover, because carbon is a conductive material that facilitates H spillover even under mild conditions<sup>23–25,45</sup>. The Ba(NO<sub>3</sub>)<sub>2</sub> decomposition through H spillover probably generated island BaO domains that were not in contact with Ru particles (Fig. 2a and Supplementary Figs. 4 and 5).

We also confirmed that using other Ba precursors, such as Ba(CH<sub>3</sub>COO)<sub>2</sub>, and using different solvents for impregnation resulted in only marginal changes in the size and location of BaO domains (Supplementary Fig. 10). However, simple thermal decomposition of Ba(NO<sub>3</sub>)<sub>2</sub> under He instead of H<sub>2</sub> produced markedly larger BaO domains, which are catalytically much less effective (Supplementary Fig. 11 and Supplementary Note 1). These results suggest that the dispersion and location of BaO are primarily determined by the decomposition mechanism of the Ba precursors (whether H spillover-assisted or not), rather than by the initial distribution and type of Ba precursor. It appears that H spillover enhances BaO dispersion on carbon surfaces, probably by increasing the rate of BaO nucleation during Ba precursor decomposition.

### Ammonia synthesis properties of catalysts

Extensive kinetic studies were conducted on the 22 carbon-supported and 2 MgO-supported Ru catalysts (with or without Ba) during NH<sub>3</sub> synthesis. Unless specified, high-purity H<sub>2</sub> and N<sub>2</sub> gases (99.999%) were

mixed as the reactant feedstock (<0.4 ppm O<sub>2</sub> and <0.7 ppm H<sub>2</sub>O). For all kinetic measurements, reactant conversion levels were kept low (<2%) to ensure that the conditions are sufficiently far from thermodynamic equilibrium. The NH<sub>3</sub> production rates of the catalysts at 573 K and 1.0 MPa are summarized in Fig. 3a. The catalysts exhibited an extremely wide range of NH<sub>3</sub> production rates (0.8–342.3 mmol g<sub>Ru</sub><sup>-1</sup> h<sup>-1</sup>), depending on the types of support and BaO promotion. This variation is remarkable, considering that all catalysts possessed Ru particles with similar size distributions (2.1–2.4 nm). With both MgO and carbon supports, BaO enhanced NH<sub>3</sub> production rates by a factor of 12.5–18.9, indicating its notable promoting effects. The NH<sub>3</sub> production rates of Ba-Ru/carbon catalysts varied widely depending on the types of carbon support. The rate increased in the order of graphite < AC < SWNT (≈MgO) < DWNT < graphene < GNF ≈ MWNTs. In the case of MWNT supports, the NH<sub>3</sub> production rate increased as the diameter of MWNTs decreased (MWNT-4 < MWNT-3 < MWNT-2 < MWNT-1). After N-doping onto MWNT-1 (N-MWNT-1), the NH<sub>3</sub> production rate increased further. Consequently, Ba-Ru/N-MWNT-1 exhibited the highest NH<sub>3</sub> production rate among all catalysts. Its NH<sub>3</sub> production rate (342.3 mmol g<sub>Ru</sub><sup>-1</sup> h<sup>-1</sup>) is 7.4-fold larger than that of Ba-Ru/MgO (46.4 mmol g<sub>Ru</sub><sup>-1</sup> h<sup>-1</sup>) and substantially outperforms other recently reported Ru catalysts under various reaction conditions (Supplementary Fig. 12 and Supplementary Note 2).

The catalysts exhibited a considerable variation in apparent activation energies (*E<sub>a</sub>*) in the range of 67.3–121 kJ mol<sup>-1</sup> (Fig. 3b and Supplementary Fig. 13). The most active catalyst, Ba-Ru/N-MWNT-1, exhibited the lowest *E<sub>a</sub>* value, while the least active catalyst, Ru/graphite, showed the highest value. Because the N<sub>2</sub> dissociation is the rate-determining



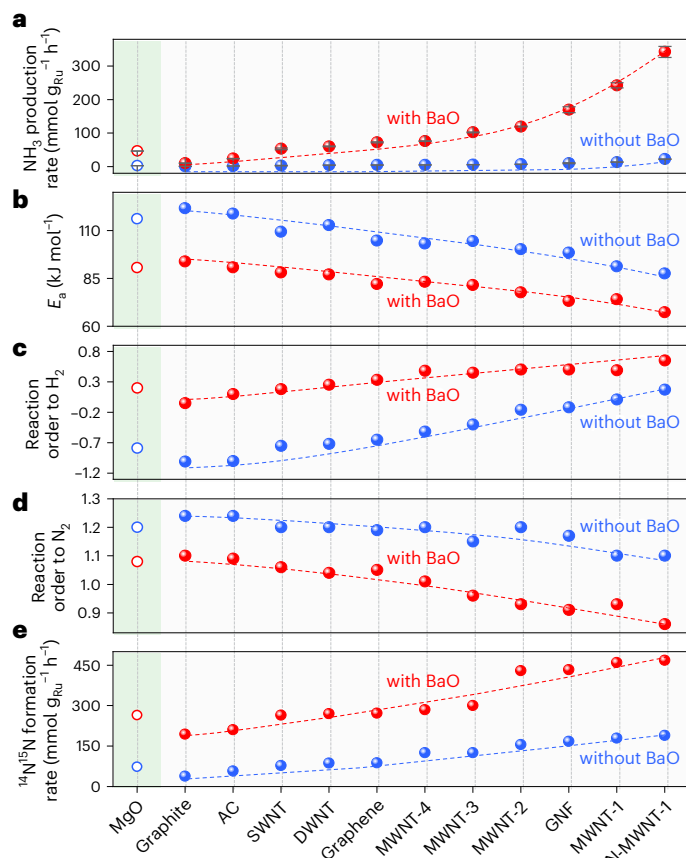


**Fig. 3 |  $\text{NH}_3$  synthesis properties of the Ru catalysts.** **a**,  $\text{NH}_3$  production rates at 573 K and a total pressure of 1.0 MPa ( $\text{H}_2/\text{N}_2 = 3$ ). Catalytic performance was measured three times, and the average with standard deviation as error bars is shown. **b–e**, Apparent activation barriers (**b**), reaction orders with respect to  $\text{H}_2$  partial pressure (**c**), reaction orders with respect to  $\text{N}_2$  partial pressure (**d**) and  $^{14}\text{N}_2$ – $^{15}\text{N}_2$  isotopic exchange rates (**e**) of the Ru catalysts at 573 K. The results for MgO-supported Ru catalysts are shown in the green area.

step for  $\text{NH}_3$  synthesis<sup>46</sup>, lower  $E_a$  values indicate more facile  $\text{N}_2$  activation. In addition, more active catalysts exhibited a larger reaction order with respect to the  $\text{H}_2$  pressure (Fig. 3c and Supplementary Fig. 14). The least active Ru/graphite exhibited a highly negative order (−1.01), indicating severe  $\text{H}_2$  poisoning, whereas the most active Ba–Ru/N-MWNT-1 showed a markedly positive order (0.65). With increasing activity, the catalysts exhibited a monotonically decreasing reaction order for  $\text{N}_2$  pressure (Fig. 3d and Supplementary Fig. 15). Thus, Ru/graphite exhibited a reaction order of 1.24, whereas Ba–Ru/N-MWNT-1 showed a reaction order of 0.86. In the  $^{14}\text{N}_2$ – $^{15}\text{N}_2$  isotopic exchange experiments, more active catalysts exhibited faster isotopic exchange (Fig. 3e), indicating more facile  $\text{N}_2$  activation. Consequently, Ba–Ru/N-MWNT-1 exhibited a 12.3-fold faster exchange rate than Ru/graphite. All these results coherently indicate that active catalysts can effectively activate  $\text{N}_2$  and alleviate hydrogen poisoning. All catalysts showed small negative orders for  $\text{NH}_3$  pressure (−0.19 to −0.18; Supplementary Fig. 16), indicating moderate binding of the product  $\text{NH}_3$  on Ru.

### Understanding the catalytic roles of BaO and carbon supports

To investigate the possible structural changes of BaO under a  $\text{H}_2$ -containing reductive atmosphere (as in  $\text{NH}_3$  synthesis conditions),  $\text{CO}_2$  TPD–MS, Raman spectroscopy and X-ray photoelectron spectroscopy (XPS) were carried out, both with and without  $\text{H}_2$  pretreatment at 673 K. When comparing the  $\text{CO}_2$  TPD–MS profiles collected after  $\text{H}_2$  and He pretreatment, all Ba–Ru/carbon catalysts exhibited a substantial

reduction in the  $\text{CO}_2$  desorption peak centred at 1,000–1,030 K after  $\text{H}_2$  pretreatment (Fig. 4a and Supplementary Fig. 17). In the Raman spectra, the  $\text{H}_2$ -pretreated catalysts showed newly appearing bands at 3,500–3,650  $\text{cm}^{-1}$  (Fig. 4b and Supplementary Fig. 18), which were assigned to BaO–H stretching vibrations<sup>47</sup>. These results suggest that H atoms produced through  $\text{H}_2$  activation on Ru can split into  $\text{H}^+$ / $\text{e}^-$  pairs, and the resulting  $\text{H}^+$  titrates basic BaO to form BaOH surface species<sup>8</sup>. According to the Ba 3d XPS (Fig. 4c and Supplementary Fig. 19), the oxidation state of Ba remains +2 after  $\text{H}_2$  pretreatment. This indicates that  $\text{e}^-$  does not transfer to non-reducible BaO, but rather accumulates in other parts of the catalysts, probably along the conductive Ru/carbon (Fig. 1b).

These observations were seemingly similar to those we previously obtained with Ba–Ru/MgO (ref. 8). However, a remarkable difference exists between the carbon- and MgO-based catalyst systems. On the MgO support, the titration of BaO with  $\text{H}^+$  occurred only at the intimate BaO–Ru interfaces, but not in island BaO domains that were not in contact with Ru (ref. 8). This can be explained by the fact that insulating MgO prevents the long-range migration of  $\text{H}^+$ / $\text{e}^-$  pairs (or H spillover), thereby making the splitting of H into  $\text{H}^+$ / $\text{e}^-$  feasible only at the BaO–Ru interfaces (Fig. 1a). It is worth recalling that the present Ba–Ru/carbon catalysts predominantly possessed separated Ru and BaO domains, yet still exhibited significant titration of BaO with  $\text{H}^+$  ions. This can be attributed to the fact that conductive carbon can facilitate the long-range migration of  $\text{H}^+$ / $\text{e}^-$  pairs, with  $\text{H}^+$  moving over the carbon surface and  $\text{e}^-$  travelling through the conduction band<sup>23–25</sup>.

To investigate the  $\text{e}^-$  accumulation in conductive Ru/carbon, the electronic structures of carbon and Ru were analysed using ultraviolet photoelectron spectroscopy (UPS) and XPS. In XPS, an Au film was used as an external reference to calibrate the binding energy scale (Au 4f<sub>7/2</sub> binding energy of 84.0 eV). The pristine carbon supports exhibited work functions ranging from 4.46 to 4.80 eV, with the lowest value observed for N-MWNT-1 and the highest for graphite (Supplementary Table 3 and Supplementary Fig. 20). When Ru/carbon and Ba–Ru/carbon catalysts were pretreated in He, their work functions were almost identical to those of the bare carbon supports (Supplementary Table 3 and Supplementary Fig. 21). This implies that the effective work function of the catalyst, a composite material, is governed by its most predominant component<sup>48</sup>, the carbon support. After  $\text{H}_2$  pretreatment, the work functions of Ru/carbon catalysts still remained similar to those of the original carbon supports (Fig. 4d, Supplementary Table 3 and Supplementary Fig. 22). Notably, when Ba–Ru/carbon catalysts were pretreated in  $\text{H}_2$ , substantial decreases in work functions (0.15–0.18 eV) were observed (Fig. 4d, Supplementary Table 3 and Supplementary Fig. 23). The reduced work function implies that the Fermi levels of the catalysts were upshifted due to increased electron density<sup>49</sup>. The  $\text{H}_2$ -pretreated Ba–Ru/carbon catalysts also exhibited redshifts in the binding energies of C 1s (Fig. 4e and Supplementary Fig. 24) and Ru 3d XPS spectra (Fig. 4f and Supplementary Fig. 25), confirming increased electron density in carbon and Ru, respectively. These results support our hypothesis that  $\text{H}^+$  is captured by BaO, while  $\text{e}^-$  accumulates in Ru/carbon in Ba–Ru/carbon catalysts under a reductive atmosphere.

Notably, Ru became increasingly enriched with  $\text{e}^-$ , showing a larger redshift in the Ru 3d<sub>5/2</sub> binding energy, as the work function of the catalysts (governed by that of carbon) decreased (Fig. 4f,g). This can be explained by the fact that carbon supports with lower work functions than Ru (4.67 eV; Supplementary Fig. 26) efficiently donate  $\text{e}^-$  to the Ru particles to align their Fermi levels. It appears that, when BaO captures  $\text{H}^+$ ,  $\text{e}^-$  accumulates in the conductive Ru/carbon, while the relative distribution of  $\text{e}^-$  between Ru and carbon is determined by the difference in their work functions. Among the catalysts, Ba–Ru/N-MWNT-1 showed the lowest work function after  $\text{H}_2$  pretreatment (4.28 eV) and, thus, the greatest  $\text{e}^-$  enrichment of Ru. This can be attributed to the fact that doping electron-rich nitrogen into a carbon

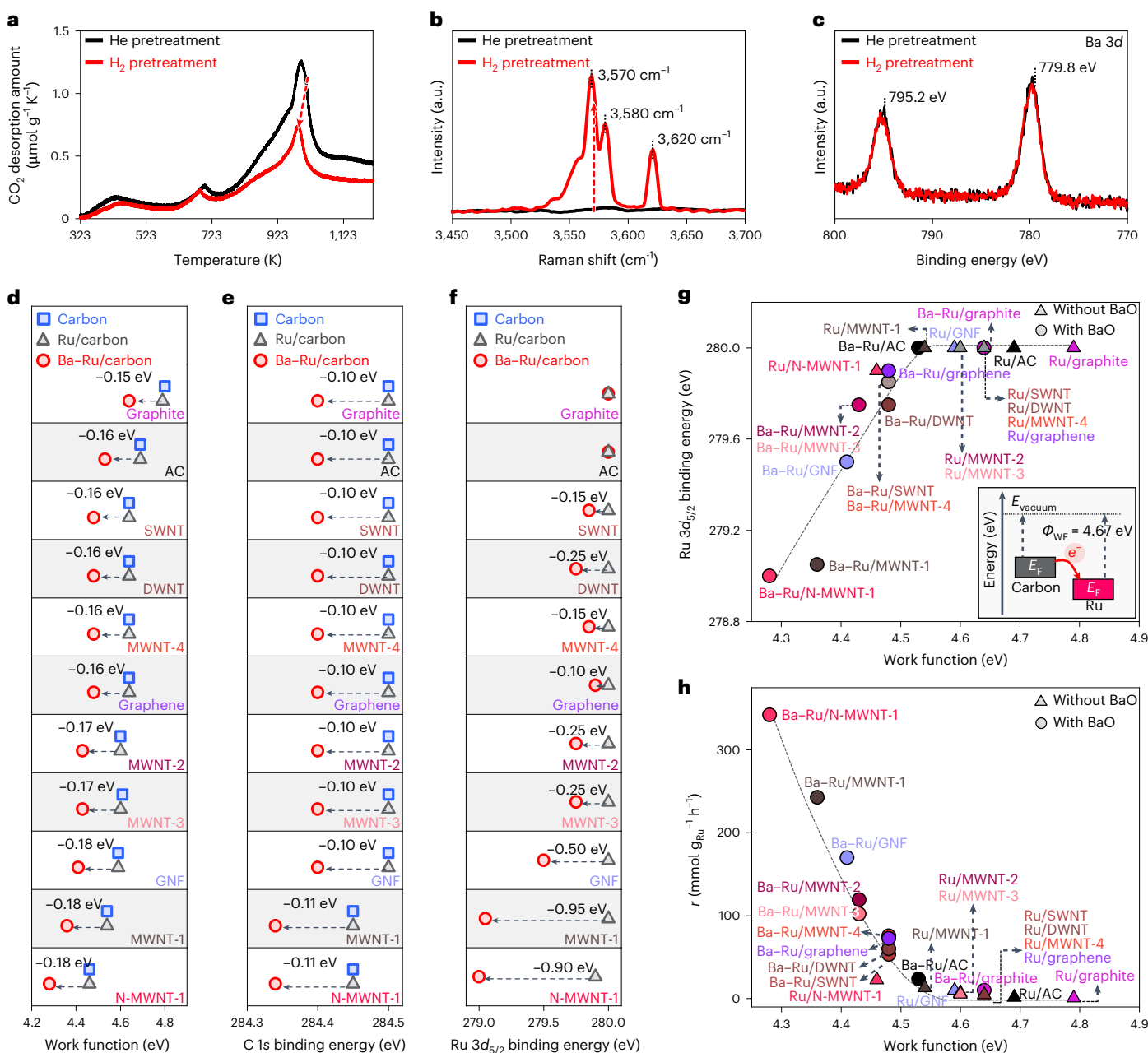


**Fig. 4 | Separate storage of H<sup>+</sup> and e<sup>-</sup> at BaO and conductive Ru/carbon.** **a–c.** CO<sub>2</sub> TPD–MS profiles (**a**), Raman spectra (**b**) and Ba 3d XPS (**c**) of Ba–Ru/N–MWNT-1 collected after He and H<sub>2</sub> pretreatment at 673 K. **d–f.** Work functions (**d**), C 1s binding energies (**e**) and Ru 3d<sub>5/2</sub> binding energies (**f**) of the carbon supports and supported Ru catalysts measured after H<sub>2</sub> pretreatment. The square symbols represent carbon, the triangles represent Ru/carbon and the circles represent Ba–Ru/carbon samples. **g, h.** Ru 3d<sub>5/2</sub> binding energies

(**g**) and NH<sub>3</sub> production rates (**h**) plotted as a function of the work functions of the catalysts after H<sub>2</sub> pretreatment. The triangle symbols represent Ru/carbon samples without BaO, and the circles represent Ba–Ru/carbon samples. The inset in **g** illustrates the electron transfer from low-work-function carbon to high-work-function Ru particles.  $\Phi_{WF}$  and  $E_F$  refer to the work function and Fermi level, respectively.

framework can effectively lower its work function<sup>30</sup>. Indeed, our additional experiments revealed that the work function of the catalysts decreases and their NH<sub>3</sub> synthesis rate increases monotonically with increasing nitrogen doping in the carbon support (Supplementary Table 4, Supplementary Figs. 27–29 and Supplementary Note 3). Given that e<sup>-</sup> enrichment of Ru is essential for activating the N≡N bond of N<sub>2</sub> via  $\pi$ -backdonation<sup>8,32–35,37</sup>, the work function of the carbon support turns out to be the most critical descriptor for the NH<sub>3</sub> production rates of the Ba–Ru/carbon catalysts, regardless of the reaction temperature between 573 K and 673 K (Fig. 4h and Supplementary Fig. 30). Other important catalytic properties, such as reaction orders with respect

to H<sub>2</sub> and N<sub>2</sub> pressures (Supplementary Fig. 31) and <sup>14</sup>N<sub>2</sub>–<sup>15</sup>N<sub>2</sub> isotopic exchange activity (Supplementary Fig. 32), also showed strong correlations with the work functions.

#### BaO loading effects and stability of Ba–Ru/N–MWNT-1

We also investigated the effects of different BaO loadings on Ru/N–MWNT-1 (Fig. 5a). As the Ba/Ru ratio increased up to 0.75, the NH<sub>3</sub> production rate increased, but thereafter it plateaued. These results indicate that increased BaO loading is helpful in enriching Ru with e<sup>-</sup> under reductive conditions, but there exists a saturation level. This behaviour is markedly different from that of the Ru/MgO system, which

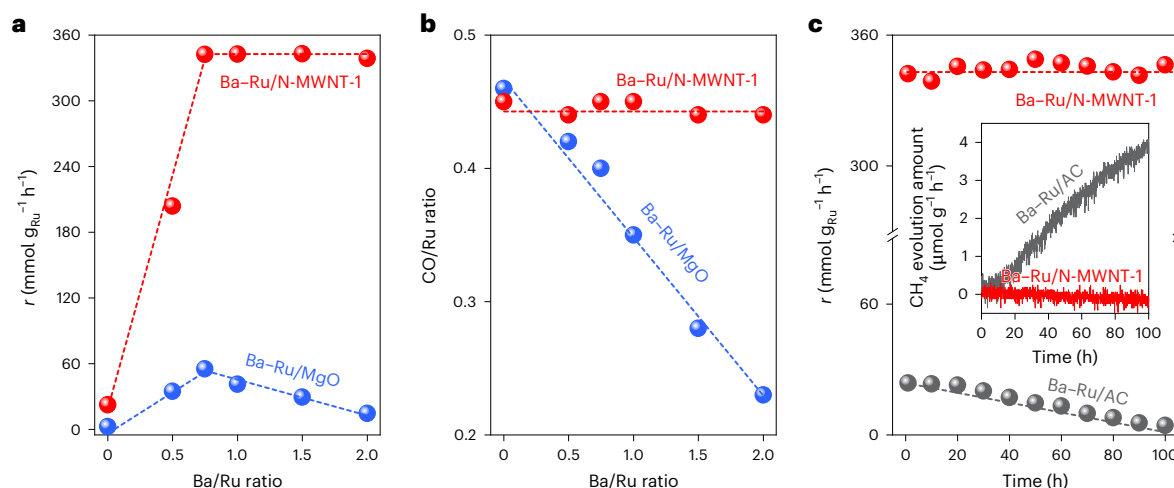


**Fig. 5 | Effects of BaO loading and long-term catalyst stability. a**, Effects of BaO loading onto Ru/N-MWNT-1 and Ru/MgO on the NH<sub>3</sub> production rate at 573 K and 1.0 MPa. **b**, CO chemisorption on Ru/N-MWNT-1 and Ru/MgO catalysts with

different BaO loadings. **c**, Long-term stabilities of Ba-Ru/N-MWNT-1 and Ba-Ru/AC, and methane formation during the NH<sub>3</sub> synthesis reaction. Both catalysts have a molar Ba/Ru ratio of 0.75.

exhibited volcano-type behaviour with respect to BaO loading (Fig. 5a). According to CO chemisorption (Fig. 5b), increasing BaO loading onto Ru/MgO monotonically decreased the number of accessible Ru site due to surface blockage. Thus, the observed volcano-type behaviour probably originated from the trade-off between increased specific activity and a decreased number of active sites as BaO loading increased. By contrast, increasing BaO loading on Ru/N-MWNT-1 did not reduce the number of accessible Ru sites (Fig. 5b) because BaO and Ru formed separate domains on the carbon surface (Fig. 2a).

It has been reported that carbon-supported Ru catalysts can suffer from methanation during NH<sub>3</sub> synthesis<sup>50</sup>. Methanation can result in the permanent loss of carbon support and cause catalyst sintering. In this context, we investigated the long-term stability of the best catalyst, Ba-Ru/N-MWNT-1 (Ba/Ru = 0.75), in comparison with that of Ba-Ru/AC, one of the most widely studied catalysts in the literature<sup>14–16,18</sup>. Ba-Ru/N-MWNT-1 exhibited a high and stable NH<sub>3</sub> production rate over 100 h (Fig. 5c), while Ba-Ru/AC showed a much lower, rapidly decreasing NH<sub>3</sub> production rate. N<sub>2</sub> adsorption and elemental analysis showed that the surface area and nitrogen content of Ba-Ru/N-MWNT-1 remained unchanged after the reaction (Supplementary Table 5). Ba-Ru/N-MWNT-1 also exhibited negligible changes in Ru and BaO dispersions, as well as in the work function (Supplementary Fig. 33). These results indicate that Ba-Ru/N-MWNT-1 is thermochemically stable during NH<sub>3</sub> synthesis. By contrast, Ba-Ru/AC exhibited a considerable decrease in surface area (Supplementary Table 5) and sintering of Ru and BaO (particularly BaO) (Supplementary Fig. 34) due to carbon degradation via methanation (Fig. 5c, inset).

We also investigated the long-term stability of Ba-Ru/N-MWNT-1 under harsher reaction conditions (Supplementary Fig. 35). Commercial reactant feedstocks can contain oxygen impurities (for example, O<sub>2</sub> and H<sub>2</sub>O), with oxygen-equivalent concentrations reaching up to 10 ppm (ref. 51). These oxygen impurities can also degrade the carbon support through the formation of CO and CO<sub>2</sub>. Given that catalyst deactivation is more severe at elevated temperatures, we tested the stability of Ba-Ru/N-MWNT-1 under a flow of a mixture of low-purity N<sub>2</sub> and H<sub>2</sub> gases (99.9%) (<45 ppm O<sub>2</sub> and <170 ppm H<sub>2</sub>O in the reactant feed) at an increased reaction temperature of 673 K for 500 h. Regardless of reactant purity, Ba-Ru/N-MWNT-1 exhibited similar activity and excellent stability, without the generation of CH<sub>4</sub>, CO or CO<sub>2</sub>. This remarkable stability can be attributed to the high crystallinity of N-MWNT (Supplementary Fig. 1), which provides great thermochemical stability.

## Conclusions

The present results demonstrate that separate Ru and BaO domains, wired by conductive carbon supports, can respectively store e<sup>-</sup> and H<sup>+</sup> after H<sub>2</sub> activation under NH<sub>3</sub> synthesis conditions. These catalysts can be considered chemical capacitors because two differently charged species, e<sup>-</sup> and H<sup>+</sup>, are separately stored by the chemical function of BaO (a strong base). The electronic promotion effects of BaO, well recognized in the literature for a long time, appear not to stem from simple inductive effects<sup>9,16</sup>, but rather from such charge capacitive effects. In particular, low-work-function carbon supports can effectively increase the electron density of the Ru catalyst particles, thereby increasing the overall NH<sub>3</sub> production rates. We believe that the development of advanced nanostructured carbon supports with lower work functions and higher crystallinity will enable the development of highly active and stable base-promoted Ru catalysts for NH<sub>3</sub> synthesis.

## Methods

### Catalyst preparation

AC (Sigma-Aldrich), graphene (RNDKOREA), graphite (Sigma-Aldrich), GNF (Carbon Nano-material Technology) and various carbon nanotubes (RNDKOREA), including SWNT, DWNT and multiwalled carbon nanotubes with diameters of 10–20 nm (MWNT-1), 20–30 nm (MWNT-2), 30–50 nm (MWNT-3) and 50–80 nm (MWNT-4), were purchased. These samples were dispersed in 200 ml of 6 M aqueous HCl solution and sonicated for 1 h at room temperature to remove metal impurities. To synthesize N-MWNT-1 with different nitrogen contents, MWNT-1 was treated with NH<sub>3</sub> at varying temperatures, both with and without HNO<sub>3</sub> pretreatment to introduce defect sites. The combination of HNO<sub>3</sub> pretreatment and lower NH<sub>3</sub> treatment temperatures resulted in enhanced nitrogen doping (Supplementary Table 4). For the typical synthesis of N-MWNT-1, 1 g of MWNT-1 was first oxidized in 100 ml of HNO<sub>3</sub> (60%, Samchun) at 373 K for 2 h. The resulting sample was collected by filtration, thoroughly washed with deionized water and dried at 373 K overnight. Subsequently, the sample was heated to 973 K (ramp: 5 K min<sup>-1</sup>) in NH<sub>3</sub> flow (100 ml min<sup>-1</sup>) and held for 2 h.

Ru was loaded onto the carbon supports via a wet impregnation method to achieve a nominal Ru loading of 5 wt%. Typically, 1 g of carbon was dispersed in a solution containing 40 g of acetone (99.5%, Sigma-Aldrich) and 0.14 g of RuCl<sub>3</sub>·3H<sub>2</sub>O (99.9%, Sigma-Aldrich). Acetone was evaporated at 303 K under vacuum. The resultant powder was further dried overnight at 323 K and subsequently reduced under H<sub>2</sub> flow at 673 K for 2 h (ramp: 2 K min<sup>-1</sup>). To prepare Ba-Ru/carbon



samples, 1.0 g of the prepared Ru/carbon samples was additionally impregnated with 0.10 g of  $\text{Ba}(\text{NO}_3)_2$  (99%, Sigma-Aldrich) dissolved in 0.055–1.5 g of deionized water and dried at 373 K to achieve a nominal Ba/Ru molar ratio of 0.75. Then, the samples were heated to 673 K for 2 h (ramp: 2 K  $\text{min}^{-1}$ ) under  $\text{H}_2$  flow.

For comparison, Ru/MgO and Ba–Ru/MgO samples were prepared using the optimized method we previously reported<sup>8</sup>. To synthesize Ru/MgO (ref. 8), 3.5 g of MgO (95%, Ducksan) and 0.22 g of NaOH (98%, Daejung) were mixed with 120 g of deionized water. A solution containing 0.48 g of  $\text{RuCl}_3 \cdot 3\text{H}_2\text{O}$  (99.9%, Sigma-Aldrich) in 20 g of deionized water was then added dropwise to the mixture while stirring vigorously. The mixture was hydrothermally treated in a Teflon-lined stainless-steel autoclave at 433 K for 24 h under tumbling (30 rpm). The solid product was recovered by filtration and thoroughly washed with deionized water. The recovered sample was dried at 373 K for 12 h, calcined in dry air at 773 K for 2 h (ramp: 2 K  $\text{min}^{-1}$ ) and reduced in  $\text{H}_2$  at 773 K for 2 h (ramp: 2 K  $\text{min}^{-1}$ ). To synthesize Ba–Ru/MgO (ref. 8), 1.0 g of Ru/MgO was impregnated with 0.10 g of  $\text{Ba}(\text{NO}_3)_2$  (99%, Sigma-Aldrich) dissolved in 0.70 g of deionized water and dried at 373 K to achieve a nominal Ba/Ru molar ratio of 0.75. The dried sample was then reduced at 773 K for 2 h (ramp: 2 K  $\text{min}^{-1}$ ) under humid  $\text{H}_2$  (4.24 kPa  $\text{H}_2\text{O}$  in  $\text{H}_2$ ).

### Characterization

The elemental compositions of the carbon supports (H, O and N) were determined by elemental analysis using a FLASH 2000 (Thermo Scientific) after thorough evacuation at 673 K for 2 h. The metal impurity contents of carbon supports (Fe, Co and Ni), as well as the Ru and Ba contents of the catalysts, were determined by inductively coupled plasma optical emission spectroscopy using an ICP-OES 720 instrument (Agilent).  $\text{N}_2$  adsorption–desorption isotherms were measured using a Belsorp-Max (BEL Japan) adsorption analyser at 77 K after vacuum degassing at 673 K. The Brunauer–Emmett–Teller surface areas were determined in the  $P/P_0$  range of 0.05–0.15 ( $P$  and  $P_0$  refer to the pressure and saturated vapor pressure of  $\text{N}_2$  at 77 K, respectively). CO chemisorption was carried out using an ASAP 2020 instrument (Micromeritics). Before analysis, all catalysts were reduced in  $\text{H}_2$  at 673 K for 3 h, followed by evacuation for 3 h at the same temperature. CO chemisorption was conducted at 323 K within a pressure range of 0.3–60 kPa. After the initial adsorption measurement, the samples were evacuated at 323 K for 1 h and the second isotherm was measured. The quantity of chemisorbed CO was determined by calculating the difference between the first and second adsorption isotherms. TEM, HAADF-STEM and elemental mapping via energy-dispersive spectroscopy were performed using a Titan Cubed G2 60–300 microscope operating at 300 kV (KAIST Analysis Center for Research Advancement, KARA), after mounting the samples on a carbon-coated copper grid (300 mesh) using an ethanolic dispersion. To determine the size distribution of Ru particles, at least 300 particles were counted. The surface-weighted mean particle size was calculated using

$$d_{\text{TEM}} = \frac{\sum n_i d_i^3}{\sum n_i d_i^2}, \quad (1)$$

where  $n_i$  represents the number of crystallites with a diameter of  $d_i$ .

Powder XRD patterns were recorded using a D2-Phaser diffractometer (Bruker) equipped with a  $\text{Cu K}\alpha$  radiation source (30 kV and 10 mA) and an LYNXEYE detector.  $\text{CO}_2$  TPD–MS profiles were collected using a BELMASS II (BEL Japan). Typically, 0.03 g of sieved particles (200–300  $\mu\text{m}$ ) were pretreated with He or  $\text{H}_2$  flow (30  $\text{ml min}^{-1}$ ) at 673 K for 2 h and cooled to 323 K.  $\text{CO}_2$  was then flowed (30  $\text{ml min}^{-1}$ ) at 323 K for 1 h, and weakly bound  $\text{CO}_2$  was desorbed by He purging for 1 h at the same temperature.  $\text{CO}_2$  TPD–MS profiles were measured from 323 to 1,273 K with a ramp rate of 10 K  $\text{min}^{-1}$  under He flow (30  $\text{ml min}^{-1}$ ). The desorbed  $\text{CO}_2$  signal was identified by the mass signal at  $m/z = 44$ . TPR–MS was conducted in a quartz plug flow reactor (inner diameter

10.5 mm) connected to an OmniStar GSD 320 quadrupole mass spectrometer (Pfeiffer Vacuum). Before the experiments, 0.1 g of sieved sample particles (200–300  $\mu\text{m}$ ) was loaded into the reactor and purged with He at 373 K for 1 h. Then, TPR–MS profiles were measured from 373 K to 873 K with a ramp rate of 2 K  $\text{min}^{-1}$  under  $\text{H}_2$  flow (50  $\text{ml min}^{-1}$ ). The desorbed  $\text{H}_2\text{O}$ ,  $\text{NH}_3$ ,  $\text{NO}_x$  ( $\text{N}_2\text{O}$ , NO and  $\text{NO}_2$ ) and  $\text{N}_2$  signals were identified by the mass signal at  $m/z = 18, 15, 30$  and 28, respectively.

Raman spectra were recorded using an ARAMIS (Horiba Jobin Yvon) with an Ar ion laser (514 nm). Before the analysis, all samples were loaded into sample chamber and pretreated in He or  $\text{H}_2$  at 673 K for 2 h. XPS was carried out using Axis-Supra (Kratos) equipped with a monochromatic Al  $\text{K}\alpha$  radiation source (1,486.7 eV). All samples were analysed without using a charge neutralizer owing to their high electrical conductivity. The energy calibration of spectrometer was conducted using an Au reference film (Au 4 $f_{7/2}$  binding energy of 84.0 eV). UPS was conducted using an Axis-Supra (Kratos) with a He I photon source (21.22 eV). The work functions were determined from the secondary electron cut-off energies ( $E_{\text{cut-off}}$ ) in the UPS spectra using

$$\text{work function} = h\nu (\text{He I photon energy}) - E_{\text{cut-off}}. \quad (2)$$

Before the XPS and UPS analysis, all samples were pretreated in He or  $\text{H}_2$  at 673 K for 2 h and placed in a sample holder inside a glovebox ( $\text{O}_2 < 1.0$  ppm,  $\text{H}_2\text{O} < 1.0$  ppm). The sample holder was moved directly from the glovebox to the connected analysis chamber without air contact.

$^{14}\text{N}_2$ – $^{15}\text{N}_2$  isotopic exchange was conducted in a quartz plug flow reactor (inner diameter 10.5 mm) connected to the OmniStar GSD 320 quadrupole mass spectrometer (Pfeiffer Vacuum). Typically, 0.3 g of sieved particles (200–300  $\mu\text{m}$ ) was loaded into the reactor, reduced at 673 K in  $\text{H}_2$  for 2 h and then purged with He for 2 h at the same temperature. After cooling to 573 K under He flow,  $^{14}\text{N}_2$ – $^{15}\text{N}_2$  mixture (10 kPa  $^{14}\text{N}_2$ /10 kPa  $^{15}\text{N}_2$ /80 kPa He) was introduced into the reactor at a flow rate of 100  $\text{ml min}^{-1}$ .

### Catalytic measurements

$\text{NH}_3$  synthesis was conducted in an Inconel plug flow reactor (inner diameter 10.9 mm). Unless specified, high-purity  $\text{H}_2$  and  $\text{N}_2$  gases (99.999%) were mixed at an  $\text{H}_2/\text{N}_2$  ratio of 3 ( $< 0.4$  ppm  $\text{O}_2$  and  $< 0.7$  ppm  $\text{H}_2\text{O}$ ) and used as reactant feedstock.  $\text{NH}_3$  production was monitored using a gas chromatograph equipped with a thermal conductivity detector and Porapak N (10 ft  $\times$  1/8 in  $\times$  2.1 mm) and Mol Sieve 5 A (6 ft  $\times$  1/8 in  $\times$  2.1 mm) columns. Typically, 0.10–4.85 g of sieved catalysts (200–300  $\mu\text{m}$ ) was loaded into the reactor and pretreated in  $\text{H}_2$  at 673 K for 2 h. After pretreatment, the reactor was adjusted to the target temperature (573–673 K) and pressurized to 1.0 MPa under a flow of the  $\text{H}_2/\text{N}_2$  mixture. For all kinetic measurements, reactant conversion levels were kept low ( $< 2\%$ ) to ensure that the conditions remained sufficiently far from thermodynamic equilibrium (equilibrium conversions are 25% and 7.1% at 573 K and 673 K, respectively, at 1.0 MPa). Apparent activation energies were determined within the temperature range of 573–673 K, and the temperature-dependent  $\text{NH}_3$  synthesis rates were measured three times for each catalyst. To analyse the reaction orders with respect to  $\text{H}_2$  and  $\text{N}_2$ , a series of reactions were performed at 0.33–0.67 MPa of  $\text{H}_2$  and 0.25–0.50 MPa of  $\text{N}_2$ , while maintaining the total pressure at 1.0 MPa with a He balance at 573 K. The reaction order for  $\text{NH}_3$  was determined in an  $\text{H}_2/\text{N}_2$  mixture ( $\text{H}_2/\text{N}_2 = 3$ ) by varying the total gas flow rate ( $F$ , space velocity: 825–42,700  $\text{ml g}^{-1} \text{h}^{-1}$ ) at 573 K and a total pressure of 1.0 MPa.

The long-term catalyst stabilities of Ba–Ru/N-MWNT-1 and Ba–Ru/AC were tested for 100 h during the  $\text{NH}_3$  synthesis reaction at 573 K and 1.0 MPa ( $\text{H}_2/\text{N}_2$  molar ratio of 3). During the reaction, the signal for  $\text{CH}_4$  evolution was monitored using the OmniStar GSD 320 quadrupole mass spectrometer (Pfeiffer Vacuum) connected to the reactor. The  $\text{CH}_4$  evolution was identified by the mass signal at  $m/z = 13$ . The long-term

stability of Ba–Ru/N-MWNT-1 was additionally investigated under harsher reaction conditions. The stability of Ba–Ru/N-MWNT-1 was tested under a flow of a mixture of low-purity (99.9%) N<sub>2</sub> and H<sub>2</sub> gases (H<sub>2</sub>/N<sub>2</sub> = 3; <45 ppm O<sub>2</sub> and <170 ppm H<sub>2</sub>O in the reactant feed) at an increased reaction temperature of 673 K for 500 h. During the reaction, the mass signals for CH<sub>4</sub>, CO and CO<sub>2</sub> (*m/z* = 13, 12 and 44, respectively) were monitored.

## Data availability

The source data for the figures are available via Zenodo at <https://doi.org/10.5281/zenodo.14636271> (ref. 52). All other data are available from the corresponding author upon reasonable request.

## References

1. Erisman, J. W., Sutton, M. A., Galloway, J., Klimont, Z. & Winiwarter, W. How a century of ammonia synthesis changed the world. *Nat. Geosci.* **1**, 636–639 (2008).
2. Wan, Z., Tao, Y., Shao, J., Zhang, Y. & You, H. Ammonia as an effective hydrogen carrier and a clean fuel for solid oxide fuel cells. *Energy Convers. Manag.* **228**, 113729 (2021).
3. Wang, M. et al. Can sustainable ammonia synthesis pathways compete with fossil-fuel based Haber–Bosch processes? *Energy Environ. Sci.* **14**, 2535–2548 (2021).
4. Smith, C., Hill, A. K. & Torrente-Murciano, L. Current and future role of Haber–Bosch ammonia in a carbon-free energy landscape. *Energy Environ. Sci.* **13**, 331–344 (2020).
5. Ye, D. & Tsang, S. C. E. Prospects and challenges of green ammonia synthesis. *Nat. Synth.* **2**, 612–623 (2023).
6. Ye, L., Nayak-Luke, R., Banares-Alcantara, R. & Tsang, E. Reaction: ‘Green’ ammonia production. *Chem* **3**, 712–714 (2017).
7. Fang, H. et al. Challenges and opportunities of Ru-based catalysts toward the synthesis and utilization of ammonia. *ACS Catal.* **12**, 3938–3954 (2022).
8. Baik, Y. et al. Splitting of hydrogen atoms into proton–electron pairs at BaO–Ru interfaces for promoting ammonia synthesis under mild conditions. *J. Am. Chem. Soc.* **145**, 11364–11374 (2023).
9. Aika, K. I., Takano, T. & Murata, S. Preparation and characterization of chlorine-free ruthenium catalysts and the promoter effect in ammonia synthesis: 3. A magnesia-supported ruthenium catalyst. *J. Catal.* **136**, 126–140 (1992).
10. Bielawa, H., Hinrichsen, O., Birkner, A. & Muhler, M. The ammonia-synthesis catalyst of the next generation: barium-promoted oxide-supported ruthenium. *Angew. Chem. Int. Ed.* **40**, 1061–1063 (2001).
11. Szmigielski, D. et al. The kinetics of ammonia synthesis over ruthenium-based catalysts: the role of barium and cesium. *J. Catal.* **205**, 205–212 (2002).
12. Siporin, S. E. & Davis, R. J. Use of kinetic models to explore the role of base promoters on Ru/MgO ammonia synthesis catalysts. *J. Catal.* **225**, 359–368 (2004).
13. Wu, S. et al. Removal of hydrogen poisoning by electrostatically polar MgO support for low-pressure NH<sub>3</sub> synthesis at a high rate over the Ru catalyst. *ACS Catal.* **10**, 5614–5622 (2020).
14. Raróg, W., Kowalczyk, Z., Sentek, J., Składanowski, D. & Zieliński, J. Effect of K, Cs and Ba on the kinetics of NH<sub>3</sub> synthesis over carbon-based ruthenium catalysts. *Catal. Lett.* **68**, 163–168 (2000).
15. Liang, C., Wei, Z., Xin, Q. & Li, C. Ammonia synthesis over Ru/C catalysts with different carbon supports promoted by barium and potassium compounds. *Appl. Catal. A* **208**, 193–201 (2001).
16. Rossetti, I., Pernicone, N. & Forni, L. Promoters effect in Ru/C ammonia synthesis catalyst. *Appl. Catal. A* **208**, 271–278 (2001).
17. Zheng, X., Zhang, S., Xu, J. & Wei, K. Effect of thermal and oxidative treatments of activated carbon on its surface structure and suitability as a support for barium-promoted ruthenium in ammonia synthesis catalysts. *Carbon* **40**, 2597–2603 (2002).
18. Guraya, M. et al. The effect of promoters on the electronic structure of ruthenium catalysts supported on carbon. *Appl. Surf. Sci.* **238**, 77–81 (2004).
19. Chen, S. Y. et al. Ammonia synthesis over cesium-promoted mesoporous-carbon-supported ruthenium catalysts: impact of graphitization degree of the carbon support. *Appl. Catal. B* **346**, 123725 (2024).
20. Nishi, M. et al. A super-growth carbon nanotubes-supported, Cs-promoted Ru catalyst for 0.1–8 MPaG ammonia synthesis. *J. Catal.* **413**, 623–635 (2022).
21. Schlögl, R. Catalytic synthesis of ammonia—a ‘never-ending story’? *Angew. Chem. Int. Ed.* **42**, 2004–2008 (2003).
22. Strait, R. Grassroots success with KAAP. *Nitrogen Methanol* **238**, 37–43 (1999).
23. Keren, E. & Soffer, A. Simultaneous electronic and ionic surface conduction of catalyst supports: a general mechanism for spillover: the role of water in the Pd-catalyzed hydrogenation of a carbon surface. *J. Catal.* **50**, 43–55 (1977).
24. Warczinski, L. & Hättig, C. How nitrogen doping affects hydrogen spillover on carbon-supported Pd nanoparticles: new insights from DFT. *J. Phys. Chem. C* **125**, 9020–9031 (2021).
25. Lee, K. et al. Engineering nanoscale H supply chain to accelerate methanol synthesis on ZnZrO<sub>x</sub>. *Nat. Commun.* **14**, 819 (2023).
26. Ago, H. et al. Work functions and surface functional groups of multiwall carbon nanotubes. *J. Phys. Chem. B* **103**, 8116–8121 (1999).
27. Shiraishi, M. & Ata, M. Work function of carbon nanotubes. *Carbon* **39**, 1913–1917 (2001).
28. Lin, Y. et al. Insights into the surface chemistry and electronic properties of sp<sup>2</sup> and sp<sup>3</sup>-hybridized nanocarbon materials for catalysis. *Chem. Commun.* **53**, 4834–4837 (2017).
29. Rut’kov, E. V., Afanas’eva, E. Y. & Gall, N. R. Graphene and graphite work function depending on layer number on Re. *Diam. Relat. Mater.* **101**, 107576 (2020).
30. Hwang, S. K. et al. Flexible multilevel resistive memory with controlled charge trap B- and N-doped carbon nanotubes. *Nano Lett.* **12**, 2217–2221 (2012).
31. Michaelson, H. B. The work function of the elements and its periodicity. *J. Appl. Phys.* **48**, 4729–4733 (1977).
32. Kitano, M. et al. Ammonia synthesis using a stable electride as an electron donor and reversible hydrogen store. *Nat. Chem.* **4**, 934–940 (2012).
33. Gong, Y. et al. Unique catalytic mechanism for Ru-loaded ternary intermetallic electrides for ammonia synthesis. *J. Am. Chem. Soc.* **144**, 8683–8692 (2022).
34. Li, J. et al. Barium oxynitride electride as highly enhanced promotor for ruthenium catalyst in ammonia synthesis: comparative study with barium oxide. *Adv. Energy Mater.* **13**, 2302424 (2023).
35. Kitano, M. et al. Essential role of hydride ion in ruthenium-based ammonia synthesis catalysts. *Chem. Sci.* **7**, 4036–4043 (2016).
36. Ooya, K. et al. Ruthenium catalysts promoted by lanthanide oxyhydrides with high hydride-ion mobility for low-temperature ammonia synthesis. *Adv. Energy Mater.* **11**, 2003723 (2021).
37. Inoue, Y. et al. Efficient and stable ammonia synthesis by self-organized flat Ru nanoparticles on calcium amide. *ACS Catal.* **6**, 7577–7584 (2016).
38. Kitano, M. et al. Self-organized ruthenium–barium core–shell nanoparticles on a mesoporous calcium amide matrix for efficient low-temperature ammonia synthesis. *Angew. Chem. Int. Ed.* **57**, 2648–2652 (2018).
39. Dahl, S. et al. Role of steps in N<sub>2</sub> activation on Ru (0001). *Phys. Rev. Lett.* **83**, 1814–1817 (1999).
40. Jacobsen, C. J. et al. Structure sensitivity of supported ruthenium catalysts for ammonia synthesis. *J. Mol. Catal. A* **163**, 19–26 (2000).



41. Honkala, K. et al. Ammonia synthesis from first-principles calculations. *Science* **307**, 555–558 (2005).
42. Szymański, G. S., Karpiński, Z., Biniak, S. & Świątkowski, A. The effect of the gradual thermal decomposition of surface oxygen species on the chemical and catalytic properties of oxidized activated carbon. *Carbon* **40**, 2627–2639 (2002).
43. Prins, R. Hydrogen spillover. Facts and fiction. *Chem. Rev.* **112**, 2714–2738 (2012).
44. Lee, S., Kim, H., Ryoo, R., Park, J. Y. & Choi, M. Hydrogen spillover in nonreducible oxides: mechanism and catalytic utilization. *Nano Res.* **15**, 10357–10365 (2022).
45. Srinivas, S. T. & Rao, P. K. Direct observation of hydrogen spillover on carbon-supported platinum and its influence on the hydrogenation of benzene. *J. Catal.* **148**, 470–477 (1994).
46. Hinrichsen, O., Rosowski, F., Muhler, M. & Ertl, G. The microkinetics of ammonia synthesis catalyzed by cesium-promoted supported ruthenium. *Chem. Eng. Sci.* **51**, 1683–1690 (1996).
47. Lutz, H. D., Eckers, W., Schneider, G. & Haeuseler, H. Raman and infrared spectra of barium and strontium hydroxides and hydroxide hydrates. *Spectrochim. Acta A* **37**, 561–567 (1981).
48. Freeouf, J. L. & Woodall, J. M. Schottky barriers: an effective work function model. *Appl. Phys. Lett.* **39**, 727–729 (1981).
49. Kanbara, S. et al. Mechanism switching of ammonia synthesis over Ru-loaded electride catalyst at metal–insulator transition. *J. Am. Chem. Soc.* **137**, 14517–14524 (2015).
50. Tsyruľnikov, P. G., Iost, K. N., Shitova, N. B. & Temerev, V. L. Methanation of the carbon supports of ruthenium ammonia synthesis catalysts: a review. *Catal. Ind.* **8**, 341–347 (2016).
51. Attari Moghaddam, A. & Krewer, U. Poisoning of ammonia synthesis catalyst considering off-design feed compositions. *Catalysts* **10**, 1225 (2020).
52. Baik, Y. et al. Electron and proton storage on separate Ru and BaO domains mediated by conductive low-work-function carbon to accelerate ammonia synthesis. *Zenodo* <https://doi.org/10.5281/zenodo.14636271> (2025).

## Acknowledgements

This work was conducted under the framework of the research and development programme of the Korea Institute of Energy Research

(grant number C4-2401, M.C.) and supported by the National Research Foundation of Korea (grant numbers RS-2024-00333937 and RS-2024-00405261, M.C.).

## Author contributions

M.C. conceived and designed this study. Y.B., S.C., Kyeongjin Lee, D.O. and Kyungho Lee prepared the materials, performed structural and catalytic characterization, and analysed the experimental results. Y.B. and M.C. wrote the paper.

## Competing interests

The authors declare no competing interests.

## Additional information

**Supplementary information** The online version contains supplementary material available at <https://doi.org/10.1038/s41929-025-01302-z>.

**Correspondence and requests for materials** should be addressed to Minkee Choi.

**Peer review information** *Nature Catalysis* thanks Chia-Min Yang and the other, anonymous, reviewer(s) for their contribution to the peer review of this work.

**Reprints and permissions information** is available at [www.nature.com/reprints](http://www.nature.com/reprints).

**Publisher's note** Springer Nature remains neutral with regard to jurisdictional claims in published maps and institutional affiliations.

Springer Nature or its licensor (e.g. a society or other partner) holds exclusive rights to this article under a publishing agreement with the author(s) or other rightsholder(s); author self-archiving of the accepted manuscript version of this article is solely governed by the terms of such publishing agreement and applicable law.

© The Author(s), under exclusive licence to Springer Nature Limited 2025